J. Fluid Mech. (2024), *vol*. 991, A4, doi:10.1017/jfm.2024.528

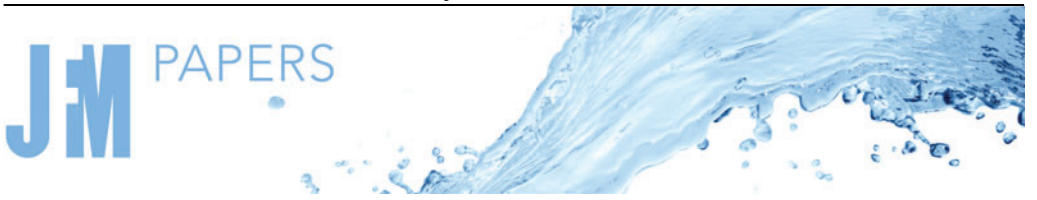

Transport scaling in porous media convection

Xiaojue Zhu[1],†, **Yifeng Fu**[1] **and Marco De Paoli**[2,3],†

[1]Max Planck Institute for Solar System Research, 37077 Göttingen, Germany

[2]Physics of Fluids Group and Max Planck Center for Complex Fluid Dynamics and J. M. Burgers Centre for Fluid Dynamics, University of Twente, P.O. Box 217, 7500AE Enschede, The Netherlands

[3]Institute of Fluid Mechanics and Heat Transfer, TU Wien, 1060 Vienna, Austria

(Received 5 March 2024; revised 18 April 2024; accepted 21 May 2024)

We present a theory to describe the Nusselt number, *Nu*, corresponding to the heat or mass flux, as a function of the Rayleigh–Darcy number, *Ra*, the ratio of buoyant driving force over diffusive dissipation, in convective porous media flows. First, we derive exact relationships within the system for the kinetic energy and the thermal dissipation rate. Second, by segregating the thermal dissipation rate into contributions from the boundary layer and the bulk, which is inspired by the ideas of the Grossmann and Lohse theory (*J. Fluid Mech.*, vol. 407, 2000; *Phys. Rev. Lett.*, vol. 86, 2001), we derive the scaling relation for *Nu* as a function of *Ra* and provide a robust theoretical explanation for the empirical relations proposed in previous studies. Specifically, by incorporating the length scale of the flow structure into the theory, we demonstrate why heat or mass transport differs between two-dimensional and three-dimensional porous media convection. Our model is in excellent agreement with the data obtained from numerical simulations, affirming its validity and predictive capabilities.

Key words: turbulent convection, convection in porous media

1. Introduction

Carbon dioxide (CO_2) sequestration is a process aimed at long-term storage of large volumes of CO_2 (Schrag 2007), primarily to mitigate climate change and support energy transition. One of the most promising sequestration strategies involves natural underground reservoirs. In this case, liquid CO_2 is injected in saline aquifers, geological porous formations located hundreds of metres beneath the Earth's surface and confined by horizontal impermeable layers (Huppert & Neufeld 2014; De Paoli 2021).

† Email addresses for correspondence: zhux@mps.mpg.de, m.depaoli@utwente.nl

Saline aquifers are filled with brine, highly salted water denser than CO_2. Because of this density difference, the injected volume of CO_2 will sit on top of the brine, and a critical configuration takes place: in case of fractures in the top confining layer of the formation, CO_2 would migrate upwards and eventually reach the upper strata up to the atmosphere (Hidalgo *et al.* 2015). However, CO_2 is partially soluble in brine and the resulting mixture, which is heavier than both starting fluids, sinks downwards through the porous rocks and safely traps the CO_2 (Emami-Meybodi *et al.* 2015; Letelier *et al.* 2023). To determine the optimal CO_2 injection rate and predict the long-time behaviour of the injected CO_2, it is therefore imperative to conduct a meticulous assessment of the flow dynamics and the associated mixing laws (MacMinn *et al.* 2012; Guo *et al.* 2021). An idealized representation of this complex system consists of a porous domain fully saturated with fluid and confined between a heated bottom plate and a cooled top plate (Hewitt, Neufeld & Lister 2012; Wen, Chang & Hesse 2018). The top-to-bottom temperature difference induces a density gradient that drives the flow. This configuration, which we label here as Rayleigh–Darcy (RD) convection, serves as a fundamental model of the aforementioned process, where the CO_2 concentration field, responsible for the density increase in the case of geological carbon sequestration, is replaced by a temperature field.

Indeed, thermal and solutal convective porous media flows can be considered equivalent and controlled by the same governing equations provided that: (i) in the temperature-driven flow, the solid phase is locally in thermal equilibrium with the liquid phase, and (ii) in the corresponding concentration-driven system, the solid is impermeable to the solute. Additional factors to be accounted for a proper comparison between these systems are the dependency of the viscosity and the fluid density with respect to the value of the scalar. While viscosity is generally weakly sensitive to temperature variations, it may be considerably affected by the local value of solute concentration. However, it has been previously shown by Hidalgo *et al.* (2012) that, in convective porous media flows, concentration-induced viscosity variations do not significantly affect the global transport properties of the system. In contrast, the shape of the density-concentration (or density-temperature) curves is shown to be crucial. For a general introduction to the RD convection, we refer to the reviews by Hewitt (2020) and De Paoli (2023). In this work, we will refer to fluid characterized by a constant viscosity and a linear dependency of density with the transported scalar (temperature).

The single control parameter in RD convection is the Rayleigh–Darcy number Ra, which indicates the relative strength between driving forces (convection) and dissipative effects (diffusion and viscosity), while the major response parameter of the system is the Nusselt number Nu, a dimensionless measure of the amount of heat (or solute) exchanged. Similar to the Rayleigh–Bénard (RB) convection (i.e. a fluid heated from below and cooled from the top, in the absence of any porous medium), in recent years, major efforts have been put into understanding the scaling relation between Nu and Ra, where Ra is intended as the thermal Rayleigh number (Ahlers, Grossmann & Lohse 2009). The classical theory (Malkus 1954; Priestley 1954; Howard 1966) posits that at significantly high Ra, the buoyancy flux should be independent of the layer's height (L). In the high-Ra regime within a porous medium, this argument predicts a linear scaling of $Nu \sim Ra$. It has also been rigorously demonstrated that the linear scaling serves as an upper bound (Doering & Constantin 1998; Otero *et al.* 2004; Wen *et al.* 2012; Hassanzadeh, Chini & Doering 2014). Interestingly, such scaling also means that the dimensional flux is independent of thermal diffusivity and, as a result, a realization of the scaling indicates the system reaches the so-called ultimate regime (Hewitt *et al.* 2012; Pirozzoli *et al.* 2021). In comparison, in RB convection, a similar argument leads to $Nu \sim Ra^{1/3}$ (Malkus 1954; Priestley 1954;

Howard 1966), different from the diffusion-free ultimate scaling $Nu \sim Ra^{1/2}$ proposed by Kraichnan (1962) and Spiegel (1963). A detailed introduction to the scalings in RB is provided by Ahlers *et al.* (2009), Chillà & Schumacher (2012) and Xia *et al.* (2023).

Direct numerical simulations (DNS) have been conducted in both two and three dimensions for RD convection to investigate heat transfer scaling at finite Ra. The two-dimensional (2-D) DNS at high Ra ($10^3 \leqslant Ra \leqslant 10^4$) by Otero *et al.* (2004) suggested a slightly sublinear $Nu(Ra)$ scaling. Subsequent DNS, as reported by Hewitt *et al.* (2012), extended up to $Ra = 4 \times 10^4$, and indicated that the scaling $Nu \sim Ra$ is asymptotically attained, albeit with a correction to the linear scaling. A simple fit, $Nu = 0.0069\,Ra + 2.75$, was proposed to accommodate the data within this range. For three-dimensional (3-D) RD convection, DNS conducted by Pirozzoli *et al.* (2021) and De Paoli *et al.* (2022) reached up to $Ra = 8 \times 10^4$ and suggested that the appropriate scaling for Nu is given by $Nu = 0.0081\,Ra + 0.067\,Ra^{0.61}$. This contrasts with an alternative fit proposed by Hewitt, Neufeld & Lister (2014), where $Nu = 0.0096\,Ra + 4.6$ was considered for the data within the range up to $Ra = 2 \times 10^4$.

It is crucial to underline that the previously mentioned corrections to the linear scaling are purely empirical in nature. This leads to the fundamental question: can we provide an explanation for these corrections and quantify them? To address this, we turn our attention to the Grossmann–Lohse (GL) theory (Grossmann & Lohse 2000, 2001), a key tool for comprehending the effective scaling of Nusselt and Reynolds numbers in relation to Ra in turbulent RB convection. The central premise of the GL theory can be summarized as follows. First, it establishes a connection between Nu and Ra by considering their relationship with the kinetic energy dissipation rate and thermal dissipation rate through exact relations. Second, the theory dissects these dissipation rates into contributions from the boundary layer (BL) and the bulk flow. In this work, we will derive corresponding exact relations for RD convection. By applying the principles of the GL theory, we can deduce the BL and bulk contributions to the thermal dissipation rate, shedding light on the origins and expressions of the corrections to the linear scaling.

2. Governing equations

We consider a fluid-saturated porous domain heated from below and cooled from above, as sketched in figure 1(*a* i). Although we discuss here the problem of a thermally driven flow in a porous medium that is locally in thermal equilibrium with the fluid, the same conclusions apply when the scalar is a solute, provided that the governing parameter (Ra) is matched. The size of the domain considered in W is the wall-parallel directions x, y and L in wall-normal direction z, along which gravity ($\boldsymbol{g}$) acts. The flow is visualized in terms of dimensionless temperature T. For sufficiently high Ra, a columnar flow structure develops both in 2-D and in 3-D flows, as one can observe from the cross-section relative to the domain midheight in figure 1(*a* ii), while the near-wall region (figure 1*a* iii) is populated by thin filamentary plumes. This structure differs significantly from the classical RB turbulence, reported in figure 1(*b*), which is controlled in the bulk by large-scale rolls. In RB convection, large-scale structures span the entire domain, with typical length scales comparable to the height of the system. In comparison, in RD convection, columnar-like structures prevail, and are characterized by length scales distinct from the system's height. This difference will be taken into account when we build up a theory for RD convection in the following sections.

Before presenting the dimensionless equations, we introduce the scaling quantities employed. The equations are made dimensionless with respect to convective flow scales

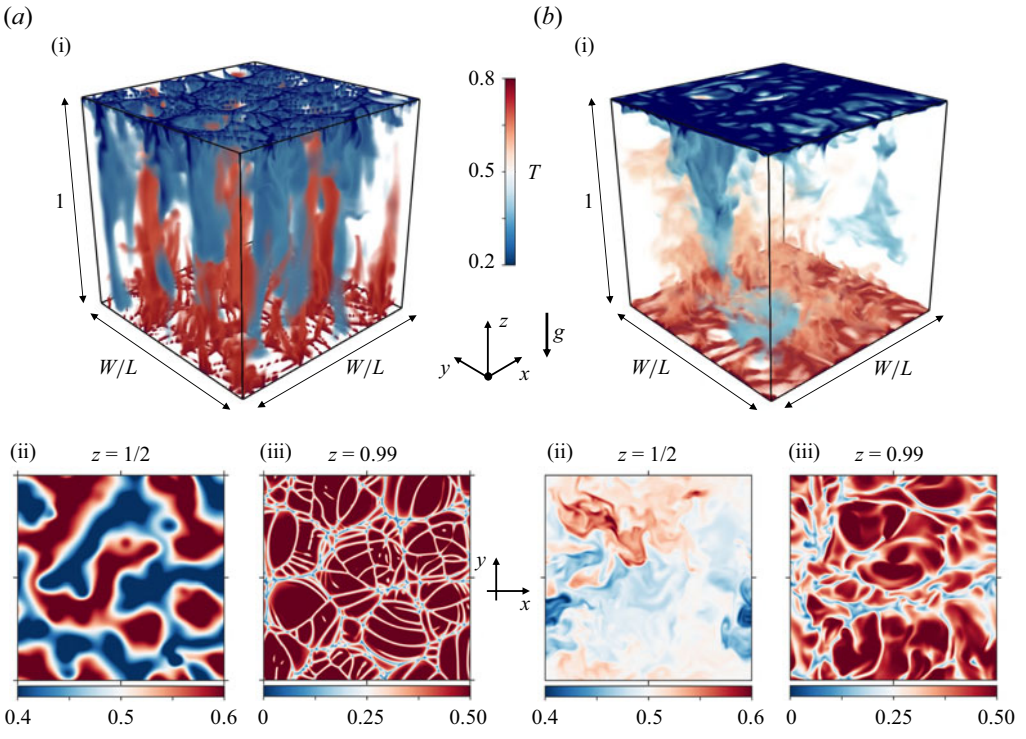

Figure 1. Instantaneous dimensionless temperature field T for convection in (a) porous media for $Ra = 10^4$, $W/L = 1$ (Pirozzoli *et al.* 2021), labelled as RD convection, and (b) in classical RB turbulence (thermal Rayleigh number 10^9, Prandtl number 1, $W/L = 1$). The temperature distribution is shown over the entire volume (a i, b i), at the centreline $z = 1/2$ (a ii, b ii) and near the upper wall (a iii, b iii).

(Pirozzoli *et al.* 2021), namely, velocities are scaled with $\mathcal{U} = \alpha g \Delta K/\nu$, where α is the thermal expansion rate, Δ the temperature difference between the bottom and the top plate, g the acceleration due to gravity, ν the kinematic viscosity and K the permeability of the porous medium, which we assume to be homogeneous and isotropic. Lengths are scaled with L and time with $\phi L/\mathcal{U}$. The dimensionless temperature is obtained as $T = (T^* - T^*_{top})/\Delta$, with T^* and T^*_{top} the dimensional temperature field and the temperature value at the top boundary, respectively. Finally, pressure is scaled by $gL(\rho^*_{top} - \rho^*_{bot})$, where the top-to-bottom fluid density difference $(\rho^*_{top} - \rho^*_{bot})$ is used. In an incompressible RD system, the heat transport is controlled by the dimensionless advection–diffusion equation (Pirozzoli *et al.* 2021),

$$\frac{\partial T}{\partial t} + \boldsymbol{u} \cdot \boldsymbol{\nabla} T = \frac{1}{Ra} \nabla^2 T, \tag{2.1}$$

where $\boldsymbol{u}$ and T are the velocity and temperature fields, respectively, t is time and Ra is the Rayleigh–Darcy number defined as

$$Ra = \frac{\alpha g \Delta K L}{\kappa \nu}. \tag{2.2}$$

In this parameter, the medium (K), domain (g, L) and fluid (α, Δ, ν, κ) properties are included, where κ is the thermal diffusivity. The momentum transport and the flow

incompressibility are accounted by the Darcy law and continuity equations,

$$\boldsymbol{u} = -(\boldsymbol{\nabla} p - T\boldsymbol{k}), \tag{2.3}$$

$$\boldsymbol{\nabla} \cdot \boldsymbol{u} = 0, \tag{2.4}$$

respectively, where p is the reduced pressure field and $\boldsymbol{k}$ is the unit vector aligned with z.

At the horizontal boundaries, we consider the temperature constant and equal to $T = 1$ at the bottom plate and $T = 0$ at the top, so that an unstable configuration is achieved and the flow is driven by convection. No-penetration boundary conditions are assumed at both plates for the velocity, while the sides are considered periodic. Equations (2.1), (2.3) and (2.4) together with these boundary conditions determine the flow dynamics, which are controlled by two dimensionless parameters, namely Ra and the horizontal domain width W/L. The latter does not appear explicitly in the equations, but may play a significant role in determining the flow structure, especially at low Ra.

3. Nusselt number and exact conservation equations

First, we will correlate the thermal (Nusselt number) and the kinetic (Péclet number) response parameters to the control parameter (Rayleigh–Darcy number), and then the thermal dissipation will be linked to the Nusselt number.

The temporal and horizontal average of (2.1) can be written as

$$\frac{\partial}{\partial z}\left(Ra\,\overline{\langle u_z T\rangle}_A - \overline{\left\langle \frac{\partial T}{\partial z}\right\rangle}_A \right) = 0. \tag{3.1}$$

The Nusselt number then reads (Letelier, Mujica & Ortega 2019; Ulloa & Letelier 2022)

$$Nu = Ra\,\overline{\langle u_z T\rangle}_A - \overline{\left\langle \frac{\partial T}{\partial z}\right\rangle}_A. \tag{3.2}$$

Here the following notations are used for different averaging procedures. Overbars $\overline{\cdots}$ correspond to the time average of a dimensionless value f, while an average over the horizontal surface and an average over the whole volume domain are denoted by $\langle\cdots\rangle_A$ and $\langle\cdots\rangle$,

$$\bar{f} = \frac{1}{\tau}\int_{t_0}^{t_0+\tau} f\,\mathrm{d}t, \tag{3.3}$$

$$\langle f\rangle_A = \frac{1}{A}\int_0^{W/L}\int_0^{W/L} f\,\mathrm{d}x\,\mathrm{d}y, \tag{3.4}$$

$$\langle f\rangle = \frac{1}{V}\int_0^{W/L}\int_0^{W/L}\int_0^{1} f\,\mathrm{d}x\,\mathrm{d}y\,\mathrm{d}z, \tag{3.5}$$

respectively, where $A = (W/L)^2$ is the dimensionless horizontal surface area and $V = (W/L)^2$ is the dimensionless volume of the whole domain based on our characteristic length scale L. Two exact relations exist in our system and can be derived from the governing equations. Using the dimensionless velocity $\boldsymbol{u}$ to dot product both sides of (2.3)

and combining with the incompressible continuity equation (2.4), we get

$$|\boldsymbol{u}|^2 = -\boldsymbol{\nabla}\cdot(p\boldsymbol{u}) + Tu_z. \tag{3.6}$$

The volume and time average of (3.6) reads

$$\overline{\langle|\boldsymbol{u}|^2\rangle} = -\frac{1}{V}\iint_{\Sigma}(p\boldsymbol{u})\cdot\hat{\boldsymbol{n}}\,\mathrm{d}S + \overline{\langle Tu_z\rangle}, \tag{3.7}$$

where Σ is the boundary surface of the domain, $\mathrm{d}S$ denotes the surface element on the boundary and $\hat{\boldsymbol{n}}$ is the normal unit vector for the surface elements. The mean power given by the pressure gradient vanishes due to the non-penetration boundary condition,

$$\frac{1}{V}\iint_{\Sigma}(p\boldsymbol{u})\cdot\hat{\boldsymbol{n}}\,\mathrm{d}S = -\frac{1}{V}\iint_{\Sigma(z=0)}pu_z\,\mathrm{d}S + \frac{1}{V}\iint_{\Sigma(z=1)}pu_z\,\mathrm{d}S = 0. \tag{3.8}$$

The mean buoyancy power in (3.7) can be written as

$$\overline{\langle Tu_z\rangle} = \frac{1}{V}\int_0^1 \overline{\langle Tu_z\rangle}_A A\,\mathrm{d}z = \frac{1}{Ra}\int_0^1\left(Nu + \overline{\left\langle\frac{\partial T}{\partial z}\right\rangle}_A\right)\mathrm{d}z. \tag{3.9}$$

Here, the last equivalence comes from the Nu definition (3.2). Since we use L as our length scale, $z\in[0,1]$. The last term in the above equation reads

$$\frac{1}{Ra}\int_0^1\overline{\left\langle\frac{\partial T}{\partial z}\right\rangle}_A\mathrm{d}z = \frac{1}{Ra}\int_0^1\frac{\partial\overline{\langle T\rangle}_A}{\partial z}\,\mathrm{d}z = \frac{1}{Ra}\left(\overline{\langle T\rangle}_A|_{z=1} - \overline{\langle T\rangle}_A|_{z=0}\right) = -\frac{1}{Ra}. \tag{3.10}$$

Reintroducing (3.10) back into (3.9), after some algebraic manipulations we get

$$\overline{\langle Tu_z\rangle} = \frac{1}{Ra}\int_0^1\left(Nu + \overline{\left\langle\frac{\partial T}{\partial z}\right\rangle}_A\right)\mathrm{d}z = \frac{1}{Ra}(Nu-1). \tag{3.11}$$

Combining (3.7), (3.8) and (3.11), we obtain an expression for the mean dimensionless velocity square,

$$\overline{\langle|\boldsymbol{u}|^2\rangle} = \frac{1}{Ra}(Nu-1). \tag{3.12}$$

We introduce the velocity scale

$$\mathcal{V} = \mathcal{U}\sqrt{\overline{\langle|\boldsymbol{u}|^2\rangle}}, \tag{3.13}$$

with $\mathcal{U} = \alpha g\Delta K/\nu$, and one finally obtains an exact relation

$$Pe^2 = (Nu-1)\,Ra \tag{3.14}$$

with

$$Pe = \frac{\mathcal{V}L}{\kappa} = Ra\,\frac{\mathcal{V}}{\mathcal{U}}, \tag{3.15}$$

where Pe is the Péclet number. The relation (3.14) aligns with the findings reported by Hassanzadeh *et al.* (2014), albeit derived from a slightly different set of equations for porous media convection. Note that for RB convection, the analogous exact relation is $\epsilon_u = \nu^3/L^4(Nu-1)\,Ra\,Pr^{-2}$, where ϵ_u is the kinetic energy dissipation rate and Pr is the Prandtl number (Ahlers *et al.* 2009). To assess the validity of (3.14), we consider the numerical

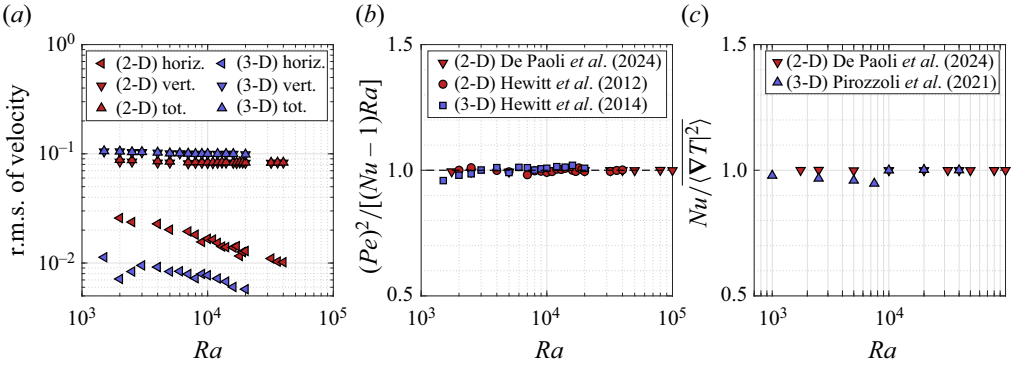

Figure 2. (*a*) The r.m.s. of velocity used to estimate the Péclet number, *Pe*. Horizontal component (r.m.s.(u)), vertical component (r.m.s.(w)) and total (defined as $\sqrt{[\text{r.m.s.}(u)]^2 + [\text{r.m.s.}(w)]^2}$ for 2-D cases, and $\sqrt{2[\text{r.m.s.}(u)]^2 + [\text{r.m.s.}(w)]^2}$ for 3-D cases) are reported; data from Hewitt *et al.* (2012, 2014). (*b*) Comparison of *Pe* compensated with $(Nu-1)\,Ra$ as from (3.14). Here *Pe* is computed with $\mathcal{V}$ defined as in (3.17) for the data from Hewitt *et al.* (2012, 2014), and as in (3.13) for data from De Paoli *et al.* (2024). (*c*) Ratio of the Nusselt number to the dimensionless thermal dissipation, derived in (3.25); data from Pirozzoli *et al.* (2021) and De Paoli *et al.* (2024).

measurements available in the literature. For 2-D flows, *Pe* is measured by De Paoli *et al.* (2024) using (3.13) and (3.15). The velocity root mean square (r.m.s.) at the centreline (2-D and 3-D) is computed by Hewitt *et al.* (2012, 2014) and reported in figure 2(*a*).

Since in all directions no mean flow exists, we have that $\mathcal{V}$ is obtained from the r.m.s. of the velocity components (u_i), namely

$$\mathcal{V} = \mathcal{U}\left(\overline{\langle [\text{r.m.s.}(u_x)]^2 + [\text{r.m.s.}(u_y)]^2 + [\text{r.m.s.}(u_z)]^2\rangle}\right)^{1/2}. \tag{3.16}$$

Assuming that the centreline flow is representative of the kinetic energy of the system, we have that

$$\mathcal{V} \approx \mathcal{U}\left(\overline{\langle [\text{r.m.s.}(u_x)]^2 + [\text{r.m.s.}(u_y)]^2 + [\text{r.m.s.}(u_z)]^2\rangle_{\Sigma(z=1/2)}}\right)^{1/2}. \tag{3.17}$$

We use this approximation to compute $\mathcal{V}$ and verify the validity of (3.14) for the data of Hewitt *et al.* (2012, 2014). We finally observe in figure 2(*b*) that (3.14) (dashed line) is in excellent agreement with the measurements obtained from the exact definition of *Pe* (2-D and $\mathcal{V}$ computed with (3.13) from De Paoli *et al.* (2024)) and also with measurements obtained from the approximated definition of *Pe* (2-D and 3-D, $\mathcal{V}$ computed with (3.17) from Hewitt *et al.* (2012, 2014)).

We will now derive an equation to correlate the mean thermal dissipation to the Nusselt number. Multiplying the dimensionless thermal advection–diffusion equation (2.1) by T, integrating over the whole domain and time-averaging, we have

$$\overline{\left\langle \frac{\partial}{\partial t}\left(\frac{T^2}{2}\right)\right\rangle} = -\overline{\langle T\boldsymbol{u}\cdot\boldsymbol{\nabla}T\rangle} + \frac{1}{Ra}\overline{\langle T\nabla^2 T\rangle}. \tag{3.18}$$

Under the assumption of a statistically steady state,

$$\overline{\left\langle \frac{\partial}{\partial t}\left(\frac{T^2}{2}\right)\right\rangle} = \frac{\partial}{\partial t}\overline{\left\langle \frac{T^2}{2}\right\rangle} = 0. \tag{3.19}$$

The first term on the right-hand side of (3.18) can be further written as

$$-\overline{\langle T\boldsymbol{u}\cdot\boldsymbol{\nabla}T\rangle}=\overline{\left\langle\frac{T^2}{2}\boldsymbol{\nabla}\cdot\boldsymbol{u}\right\rangle}-\overline{\left\langle\boldsymbol{\nabla}\cdot\left(\boldsymbol{u}\frac{T^2}{2}\right)\right\rangle}=-\frac{1}{V}\iint_{\Sigma}\left(\boldsymbol{u}\frac{T^2}{2}\right)\cdot\hat{\boldsymbol{n}}\,\mathrm{d}S=0. \tag{3.20}$$

Here we employed again continuity (2.4) and the no-penetration boundary condition. The second term on the right-hand side of (3.18) reads

$$\frac{1}{Ra}\overline{\langle T\nabla^2 T\rangle}=\frac{1}{Ra}\left[\overline{\left\langle\nabla^2\left(\frac{T^2}{2}\right)\right\rangle}-\overline{\langle|\boldsymbol{\nabla}T|^2\rangle}\right]. \tag{3.21}$$

Combining results from (3.18)–(3.21), one obtains

$$\overline{\langle|\boldsymbol{\nabla}T|^2\rangle}=\overline{\left\langle\nabla^2\left(\frac{T^2}{2}\right)\right\rangle}. \tag{3.22}$$

We can use the following procedure to further simplify the right-hand side of (3.22):

$$\overline{\left\langle\nabla^2\left(\frac{T^2}{2}\right)\right\rangle}=\frac{1}{V}\iint_{\Sigma}\left(\overline{T\boldsymbol{\nabla}T}\right)\cdot\hat{\boldsymbol{n}}\,\mathrm{d}S \tag{3.23}$$

$$=\frac{A}{V}\left(\overline{\left\langle T\frac{\partial T}{\partial z}\right\rangle}_{\Sigma(z=1)}-\overline{\left\langle T\frac{\partial T}{\partial z}\right\rangle}_{\Sigma(z=0)}\right)=Nu\,. \tag{3.24}$$

Here we considered that $V=A=(W/L)^2$, applied the boundary conditions for T and u_z, as well as the Nu definition (3.2). Combining (3.22) and (3.24), we get

$$\overline{\langle|\boldsymbol{\nabla}T|^2\rangle}=Nu, \tag{3.25}$$

where $\overline{\langle|\boldsymbol{\nabla}T|^2\rangle}$ represents the dimensionless mean thermal dissipation. This relation, which holds also for RB convection (Ahlers *et al.* 2009), has been also presented before for RD flows (Otero *et al.* 2004; Hidalgo *et al.* 2012; De Paoli 2023) and for Hele-Shaw convection the limit of infinitely thin domains (Letelier *et al.* 2019; Ulloa & Letelier 2022). The ratio of the Nusselt number to the dimensionless thermal dissipation is compared in figure 2(*c*) for the numerical results of Pirozzoli *et al.* (2021) and De Paoli *et al.* (2024). We observe that, also in this case, the agreement between theory and simulations is good, confirming the validity of (3.25). Finally, one obtains the dimensional thermal dissipation rate,

$$\epsilon=\kappa\frac{\Delta^2}{L^2}\overline{\langle|\boldsymbol{\nabla}T|^2\rangle}=\kappa\frac{\Delta^2}{L^2}Nu\,. \tag{3.26}$$

Equations (3.14) and (3.26) represent the two exact relations we derived in our system.

4. Application of GL theory and scaling relation for the Nusselt number

With the two exact relations derived in the previous section, we can now apply the main ideas of the GL theory to RD convection. The key idea of the GL theory (Grossmann & Lohse 2000, 2001) is to split the kinetic and thermal dissipation rates into contributions from the BLs and bulk. In RD convection, the procedure becomes even simpler than in

RB, as only the thermal dissipation rate appears in the exact relations. We separate the mean thermal dissipation as

$$\epsilon = \epsilon_{BL} + \epsilon_{bulk}, \tag{4.1}$$

and apply the respective scaling relations for ϵ_{BL} and ϵ_{bulk}, based on the BL theory and fully developed flow in the bulk. The horizontal- and time-averaged profiles of temperature, shown in figure 3(*a*), confirm that the flow can be split into two distinct regions: a well-mixed bulk with nearly uniform properties, and a thin BL characterized by a linear temperature profile, the slope of which is unitary when z is rescaled with Nu (figure 3*b*). The thickness of this BL, λ/L, can be determined as the distance from the wall at which the linear function fitting the temperature profile in the bulk ($0.4 \leqslant z \leqslant 0.6$) intersects the near-wall temperature fit. The measurement procedure is illustrated in figure 3(*c*), where the intersection is marked by the bullet. The Nusselt number sets the thickness of the BL $\lambda/L = 1/(2\,Nu)$ (De Paoli *et al.* 2022). In RD convection, it has been proposed by Otero *et al.* (2004) that the thermal BL thickness scales as $\lambda/L \sim Ra^{-1}$ (consistent with $Nu \sim Ra$, from the classical theory (Malkus 1954; Priestley 1954; Howard 1966) and the upper bound scaling derived by Doering & Constantin (1998)). As illustrated in figure 3(*d*), this approximation is verified. Although both in 2-D and 3-D cases the thermal BL thickness follows $\lambda/L \sim Ra^{-1}$, the prefactor differs (see figure 3*d*). This discrepancy arises from the distinct flow structures in 2-D and 3-D cases. In 3-D cases, owing to the additional degree of freedom compared with the 2-D case, plumes can freely move and reorganize towards the most efficient configuration, resulting in a different value of Nu. Consequently, the BL thickness also varies. This phenomenon is analogous to RB convection, where 2-D and 3-D flows exhibit different BL thicknesses due to variations in Nu (Van Der Poel, Stevens & Lohse 2013).

The profiles of dimensionless thermal dissipation $\overline{\langle|\boldsymbol{\nabla} T|^2\rangle_A}$ obtained from De Paoli *et al.* (2022) are shown in figure 4(*a*) for different values of the Rayleigh number. In the inset, the dissipation is rescaled by the respective Nusselt number, and shown up to 1. We observe that the BL contribution to the dissipation is more pronounced as Ra is increased. A more quantitative description is provided in the following. The thermal dissipation rate in the BL scales as $\sim \kappa(\Delta/\lambda)^2$. Therefore, taking into account the layer extension ($\lambda/L \sim Ra^{-1}$), the BL contribution towards the total thermal dissipation rate reads

$$\epsilon_{BL} \sim \kappa \frac{\Delta^2}{\lambda^2}\frac{\lambda}{L} \sim \kappa \frac{\Delta^2}{L^2} Ra\,. \tag{4.2}$$

Assuming the flow in the bulk is well mixed (Grossmann & Lohse 2000; Bader & Zhu 2023; Song, Shishkina & Zhu 2024), we get

$$\epsilon_{bulk} \sim \frac{\mathcal{V}\theta^2}{\ell}. \tag{4.3}$$

Here, $\mathcal{V}$ and θ are the typical velocity and temperature scales, respectively. The characteristic length scale is ℓ, defined as the wavelength associated with the power-averaged mean wavenumber at the midheight ($\bar{k}$), i.e. $\ell/L = 2\pi/\bar{k}$. In numerical simulations, $\bar{k}$ is obtained from the time-averaged spectrum of the temperature field at $z = 1/2$ (Hewitt *et al.* 2014). The importance of ϵ_{BL} and ϵ_{bulk} relative to the total dissipation ϵ, is reported in figure 4(*b*) for 3-D RD convection (De Paoli *et al.* 2022). Here, ϵ_{BL} and ϵ_{bulk} are obtained from the profiles, and represent the mean value within the respective regions. In RB, to derive the scalings, the length scale is assumed to be the

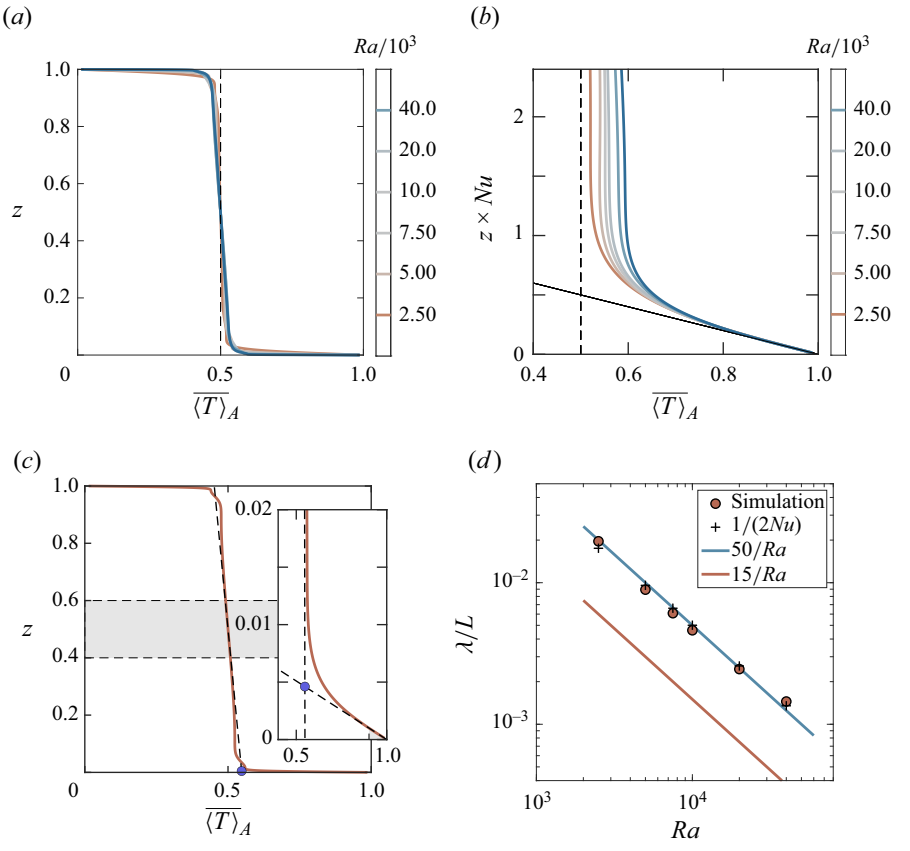

Figure 3. (*a*) Horizontal- and time-averaged profiles of temperature are shown for different Ra (De Paoli *et al.* 2022). The near-wall region is magnified in (*b*), where the wall-normal coordinate is rescaled with Nu. The profiles are self-similar, and in the BL follow a linear behaviour (solid line) with unitary slope. (*c*) The thickness of the BL is determined as the distance from the wall of the intersection between the linear profile fitting the bulk ($0.4 \leqslant z \leqslant 0.6$) and the near-wall regions ($z \leq 0.1\,Nu\,/\,Ra$). The case relative to $Ra = 10^4$ is reported. A close-up view of the near-wall region is shown in the inset. (*d*) Thickness of the thermal BL λ/L as a function of the Rayleigh number. The 3-D measurements computed as discussed (bullets) are very well fitted by the correlation $50/\,Ra$. The correlation proposed for 2-D flows by Otero *et al.* (2004) ($\lambda/L \sim 15/\,Ra$) is also reported, as well as the value obtained from the Nusselt number $\lambda/L = 1/(2\,Nu)$; data from De Paoli *et al.* (2022).

height of the domain L, which makes sense as there exist large-scale rolls. However, here in RD, the typical flow structures are columnar-like, making the length scale ℓ different from L. This difference is clearly visible in figures 1(*a* i) and 1(*b* i). From the definition of Nu (3.2) and assuming that in the bulk, $\theta \sim Nu(\kappa\,\Delta)/(\mathcal{V}L)$, and when Nu only comes from the fluctuation in the bulk, $\theta \sim (\epsilon_{bulk}/\mathcal{V})(L/\Delta)$, we get

$$\epsilon_{bulk} \sim \kappa \frac{\Delta^2}{L^2} Pe \frac{\ell}{L}. \tag{4.4}$$

The same bulk scaling has also been reported for rapidly rotating convection (Song *et al.* 2024) and magnetoconvection with strong vertical magnetic fields (Bader & Zhu 2023). In all these three systems, in the bulk there exists a new horizontal dominant length scale that is different from the height of the domain. In each of these three systems,

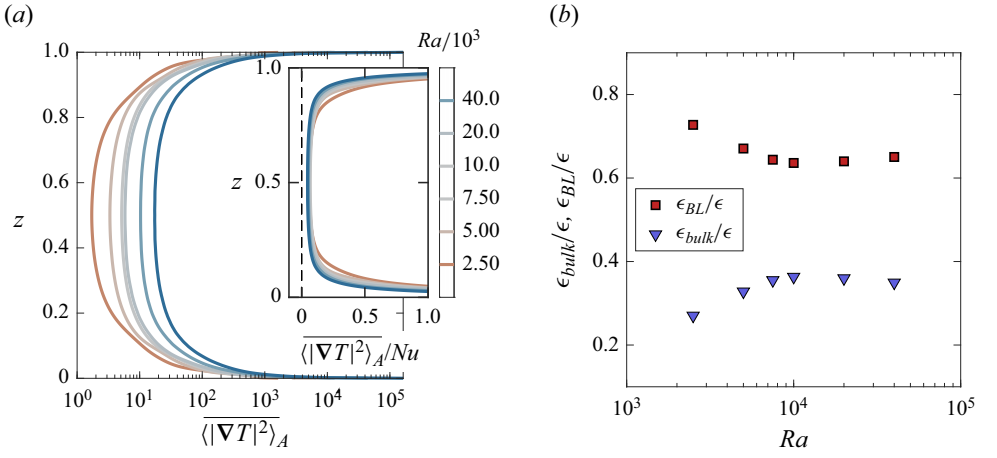

Figure 4. (*a*) Horizontal- and time-averaged profiles of dimensionless thermal dissipation, $\overline{\langle|\nabla T|^2\rangle_A}$, are shown for different Ra (De Paoli *et al.* 2022). In the inset, the dissipation is rescaled by the respective Nusselt number, and shown up to $\overline{\langle|\nabla T|^2\rangle_A}/Nu = 1$. The BL contribution to the dissipation is more pronounced as Ra is increased. (*b*) Contributions to the mean scalar dissipation ϵ within the BL (ϵ_{BL}) and in the bulk region (ϵ_{bulk}); data are from De Paoli *et al.* (2022).

a new dominant length scale emerges, distinct from the domain's height. This disparity constitutes a significant deviation from the original GL theory.

Determining the dominant wavelength in RD convection is a challenging task. The reason is linked to the complex way in which the dynamic near-wall flow structures interact with the stationary, large-scale columnar plumes controlling the bulk. A detailed review is provided by Hewitt (2020), which we summarize here with additional details including later results (De Paoli *et al.* 2022). In 3-D cases, using asymptotic stability theory, Hewitt & Lister (2017) derived that

$$\ell/L \sim Ra^{-1/2} \quad \text{(3-D)}. \tag{4.5}$$

Numerical simulations by Hewitt *et al.* (2014) and De Paoli *et al.* (2022), best fitted by scaling exponents of -0.52 and -0.49, respectively, agree well with this prediction (see also figure 5*a*). Therefore, we employ this scaling relation ($\ell/L \sim Ra^{-1/2}$) for the centreline in 3-D cases. The situation is more complex in 2-D cases. Hewitt, Neufeld & Lister (2013*b*) derived analytically the scaling relation

$$\ell/L \sim Ra^{-5/14} \quad \text{(2-D)}. \tag{4.6}$$

Wen, Corson & Chini (2015) have shown that for $Ra \leq 19\,976$ the centreline dominant length scale is well approximated by $\ell/L \sim Ra^{-0.40}$. However, one can observe in figure 5(*b*) that when $Ra \geq 39\,716$, the interplume spacing measured by Wen *et al.* (2015) is not unique. The conclusion is that in 2-D RD convection, at $Ra \geq 39\,716$, a precise scaling remains to be established by running simulations in very wide domains and for very long times. In view of this, we consider the scaling proposed by Hewitt *et al.* (2013*b*), which represents the best theoretical prediction available, to be valid. Therefore, combining (4.4) with (3.14), (4.5) and (4.6), we get

$$\epsilon_{bulk} \sim \kappa \frac{\Delta^2}{L^2} Nu^{1/2} \quad \text{(3-D)}, \tag{4.7}$$

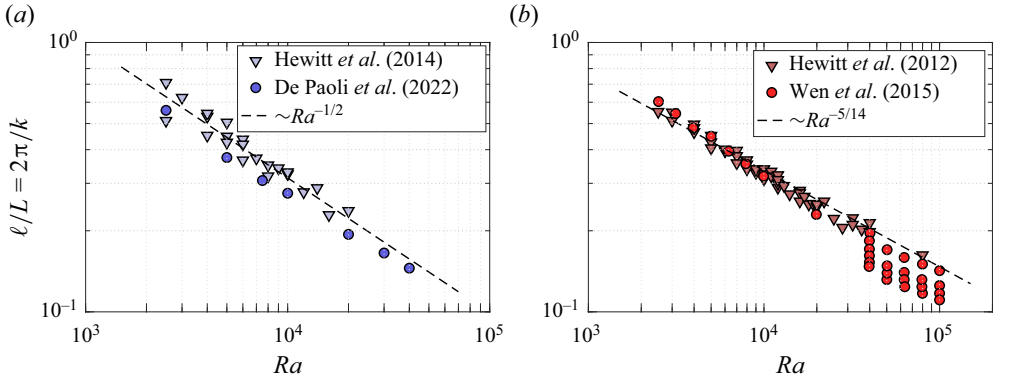

Figure 5. Dominant length scales ℓ/L in the bulk ($z = 1/2$) for (*a*) 3-D (Hewitt *et al.* 2014; De Paoli *et al.* 2022) and (*b*) 2-D (Hewitt *et al.* 2012; Wen *et al.* 2015) simulations. Theoretical scaling relations defined in (4.5) and (4.6), corresponding to 3-D and 2-D flows, respectively, are also indicated (dashed lines).

and

$$\epsilon_{bulk} \sim \kappa \frac{\Delta^2}{L^2} Nu^{1/2}\, Ra^{1/7} \quad \text{(2-D)}. \tag{4.8}$$

Finally, combining (3.26), (4.1), (4.2), (4.7) and (4.8), we reach an expression for Nu as a function of Ra for the 3-D and the 2-D cases, as follows:

$$Nu = A_3\, Ra + B_3\, Nu^{1/2} \quad \text{(3-D)}, \tag{4.9}$$

$$Nu = A_2\, Ra + B_2\, Nu^{1/2}\, Ra^{1/7} \quad \text{(2-D)}. \tag{4.10}$$

As reported in figure 6, these scaling relations fit very well the data obtained from numerical simulations, both in the 2-D and in the 3-D cases. The values of the coefficients A_2, A_3, B_2, B_3, indicated in figure 6, are obtained as best fitting from the data shown, representing the numerical results available and with $Ra > 2 \times 10^3$. The choice of considering values larger than this threshold is motivated by the flow topology: at low Ra the bulk flow structure is not columnar, as it is dominated by large-scale convective rolls (Graham & Steen 1994), and therefore our theory does not apply. The expressions of Nu derived in (4.9) and (4.10) take the form of a linear scaling with a sublinear correction. The linear scaling was previously proposed for 2-D (Hewitt *et al.* 2012) and 3-D (Hewitt *et al.* 2014) flows. The scaling proposed here provides similar results to the linear scaling with sublinear corrections proposed for the 3-D case by Pirozzoli *et al.* (2021). However, in this case one fitting parameters fewer is used, i.e. all scaling exponents are known. The good agreement of the present scaling relations with the numerical measurements available in the literature suggests that the theory proposed is indeed valid and promising for higher Ra. The RD system is completely defined by two parameters, namely the Rayleigh number Ra and the aspect ratio W/L. In 3-D flows at high-Ra, it has been observed that all major flow statistics converge for an aspect ratio of $W/L = 1$ (De Paoli *et al.* 2022). This differs in 2-D systems: also at high Ra and due to the additional lateral confinement, the aspect ratio may have an influence on ℓ (Wen *et al.* 2015). Therefore, it may be required to take W/L into account in the present theory to better describe the transport properties in 2-D RD flows. To this aim and also to assess the physics of the scaling prefactors, additional simulations in large domains and at larger Ra are needed.

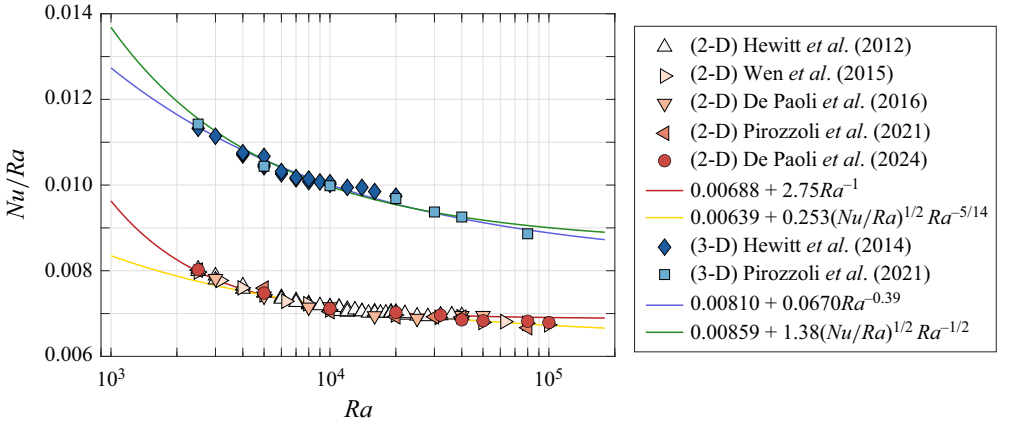

Figure 6. Compensated Nusselt number as a function of Rayleigh number. Results are for 2-D (Hewitt *et al.* 2012; Wen *et al.* 2015; De Paoli, Zonta & Soldati 2016; Pirozzoli *et al.* 2021; De Paoli *et al.* 2024) and 3-D (Hewitt *et al.* 2014; Pirozzoli *et al.* 2021) simulations. New fitting curves are obtained considering all data with $Ra > 2 \times 10^3$, with numerical values of the coefficients being $A_2 = (6.386 \pm 0.007) \times 10^{-3}$, $B_2 = 0.2533 \pm 0.0050$ and $A_3 = (8.592 \pm 0.033) \times 10^{-3}$, $B_3 = 1.376 \pm 0.059$. The coefficients of determination (R^2) for the best fitting curves provided are 0.991 and 0.999 in the 2-D and in the 3-D cases, respectively.

5. Conclusions

In summary, we have established two exact relationships, one pertaining to the Péclet number and the other to the thermal dissipation rate, in the context of Rayleigh–Darcy (RD) convection – a fundamental system for heat and mass transport in porous media. Inspired by previous models developed for RB convection (Grossmann & Lohse 2000, 2001), we have formulated a scaling theory for heat transfer in 2-D and 3-D RD flows, where the Nusselt number is expressed as a function of the Rayleigh number as described by (4.9) and (4.10). This theory enables us to provide a theoretical explanation to the sublinear empirical corrections proposed in prior studies (Pirozzoli *et al.* 2021). Our investigations, supported by both the 2-D and 3-D literature results, confirm the validity of the proposed theory. Moreover, by taking the length scale of the flow structures into account, we also shed new light on the physical origins of the disparities in scaling relations between 2-D and 3-D RD convection.

Our findings are relevant to convective flows in homogeneous and isotropic porous media where the top-to-bottom density difference is defined. However, these hypotheses represent idealized conditions not taking into account additional flow features that occur in realistic processes, such as hydrodynamic dispersion (Liang *et al.* 2018; Tsinober *et al.* 2022; Tsinober, Shavit & Rosenzweig 2023), medium heterogeneity (Simmons, Fenstemaker & Sharp 2001; Dentz, Hidalgo & Lester 2023), anisotropy (Ennis-King, Preston & Paterson 2005; De Paoli *et al.* 2016) and alternative flow configurations (Hidalgo *et al.* 2012; De Paoli, Zonta & Soldati 2017; Letelier *et al.* 2023). Nonetheless, present findings represent a crucial step required to develop a robust and physically sound theory for convection in porous media flows, which can be further expanded to include the presence of the different variations mentioned above. We consider for instance the sequestration of carbon dioxide in saline aquifers. Such a system is usually modelled as a rectangular domain initially filled with brine and confined by two horizontal low-permeability layers, and therefore it is assumed to be impermeable at the bottom boundary (no-flux) (Huppert & Neufeld 2014). Here, the solute enters from the top, in

correspondence of which the concentration of CO_2 is constant. This flow configuration, defined as 'one-sided' (Hewitt, Neufeld & Lister 2013*a*) or 'semi-infinite' (Ennis-King *et al.* 2005), is subject to a transient behaviour: the average CO_2 concentration within the system will increase over time, and it will be progressively harder to keep dissolving solute. In quantitative terms this means that, after a short initial phase in which dissolution increases due to the formation and growth of the fingers, the flux of solute through the top boundary will later reduce as a result of the saturation of the domain. The dynamics of such a system has been thoroughly characterized (Slim 2014), and it is shown to be quantitatively related to the dynamics observed in RD convection (Hewitt *et al.* 2013*a*; De Paoli *et al.* 2017). In order to describe the evolution of the one-sided system with a simple box-model, accurate predictions of the transport scaling in RD convection are essential. In the presence of high-permeability formations such as the Utsira Sand reservoir at Sleipner (Bickle *et al.* 2007), the Rayleigh–Darcy number may be as high as 6×10^5 (Hewitt *et al.* 2013*a*), which is beyond current numerical capabilities. As a result, the theoretical results provided in our work will play a crucial role as a tool to determine the long-term evolution of flows in semi-infinite domains.

Funding. We gratefully acknowledge the financial support from the Max Planck Society, the German Research Foundation through grants 521319293 and 540422505, the Alexander von Humboldt Foundation and the Daimler Benz Foundation. This project has also received funding from the European Union's Horizon Europe research and innovation programme under the Marie Sklodowska–Curie grant agreement no. 101062123.

Declaration of interests. The authors report no conflict of interest.

Author ORCIDs.
Xiaojue Zhu https://orcid.org/0000-0002-7878-0655;
Yifeng Fu https://orcid.org/0009-0006-6332-045X;
Marco De Paoli https://orcid.org/0000-0002-4709-4185.

References

Ahlers, G., Grossmann, S. & Lohse, D. 2009 Heat transfer and large scale dynamics in turbulent Rayleigh–Bénard convection. *Rev. Mod. Phys.* **81** (2), 503.

Bader, S.H. & Zhu, X. 2023 Scaling relations in quasi-static magnetoconvection with a strong vertical magnetic field. *J. Fluid Mech.* **976**, A4.

Bickle, M., Chadwick, A., Huppert, H.E., Hallworth, M. & Lyle, S. 2007 Modelling carbon dioxide accumulation at Sleipner: implications for underground carbon storage. *Earth Planet. Sci. Lett.* **255** (1), 164–176.

Chillà, F. & Schumacher, J. 2012 New perspectives in turbulent Rayleigh–Bénard convection. *Eur. Phys. J.* E **35**, 1–25.

De Paoli, M. 2021 Influence of reservoir properties on the dynamics of a migrating current of carbon dioxide. *Phys. Fluids* **33** (1), 016602.

De Paoli, M. 2023 Convective mixing in porous media: a review of Darcy, pore-scale and Hele-Shaw studies. *Eur. Phys. J.* E **46** (12), 129.

De Paoli, M., Pirozzoli, S., Zonta, F. & Soldati, A. 2022 Strong Rayleigh–Darcy convection regime in three-dimensional porous media. *J. Fluid Mech.* **943**, A51.

De Paoli, M., Yerragolam, G.S., Lohse, D. & Verzicco, R. 2024 A finite difference solver for numerical simulations of convective porous media flows (in preparation).

De Paoli, M., Zonta, F. & Soldati, A. 2016 Influence of anisotropic permeability on convection in porous media: implications for geological CO_2 sequestration. *Phys. Fluids* **28** (5), 056601.

De Paoli, M., Zonta, F. & Soldati, A. 2017 Dissolution in anisotropic porous media: modelling convection regimes from onset to shutdown. *Phys Fluids* **29** (2), 026601.

Dentz, M., Hidalgo, J.J. & Lester, D. 2023 Mixing in porous media: concepts and approaches across scales. *Transp. Porous Med.* **146** (1–2), 5–53.

DOERING, C.R. & CONSTANTIN, P. 1998 Bounds for heat transport in a porous layer. *J. Fluid Mech.* **376**, 263–296.

EMAMI-MEYBODI, H., HASSANZADEH, H., GREEN, C.P. & ENNIS-KING, J. 2015 Convective dissolution of CO_2 in saline aquifers: progress in modeling and experiments. *Intl J. Greenh. Gas Control* **40**, 238–266.

ENNIS-KING, J., PRESTON, I. & PATERSON, L. 2005 Onset of convection in anisotropic porous media subject to a rapid change in boundary conditions. *Phys. Fluids* **17** (8), 084107.

GRAHAM, M.D. & STEEN, P.H. 1994 Plume formation and resonant bifurcations in porous-media convection. *J. Fluid Mech.* **272**, 67–90.

GROSSMANN, S. & LOHSE, D. 2000 Scaling in thermal convection: a unifying theory. *J. Fluid Mech.* **407**, 27–56.

GROSSMANN, S. & LOHSE, D. 2001 Thermal convection for large Prandtl numbers. *Phys. Rev. Lett.* **86** (15), 3316.

GUO, R., SUN, H., ZHAO, Q., LI, Z., LIU, Y. & CHEN, C. 2021 A novel experimental study on density-driven instability and convective dissolution in porous media. *Geophys. Res. Lett.* **48** (23), e2021GL095619.

HASSANZADEH, P., CHINI, G.P. & DOERING, C.R. 2014 Wall to wall optimal transport. *J. Fluid Mech.* **751**, 627–662.

HEWITT, D.R. 2020 Vigorous convection in porous media. *Proc. Math. Phys. Engng Sci.* **476** (2239), 20200111.

HEWITT, D.R. & LISTER, J.R. 2017 Stability of three-dimensional columnar convection in a porous medium. *J. Fluid Mech.* **829**, 89–111.

HEWITT, D.R., NEUFELD, J.A. & LISTER, J.R. 2012 Ultimate regime of high Rayleigh number convection in a porous medium. *Phys. Rev. Lett.* **108** (22), 224503.

HEWITT, D.R., NEUFELD, J.A. & LISTER, J.R. 2013*a* Convective shutdown in a porous medium at high Rayleigh number. *J. Fluid Mech.* **719**, 551–586.

HEWITT, D.R., NEUFELD, J.A. & LISTER, J.R. 2013*b* Stability of columnar convection in a porous medium. *J. Fluid Mech.* **737**, 205–231.

HEWITT, D.R., NEUFELD, J.A. & LISTER, J.R. 2014 High Rayleigh number convection in a three-dimensional porous medium. *J. Fluid Mech.* **748**, 879–895.

HIDALGO, J.J., DENTZ, M., CABEZA, Y. & CARRERA, J. 2015 Dissolution patterns and mixing dynamics in unstable reactive flow. *Geophys. Res. Lett.* **42** (15), 6357–6364.

HIDALGO, J.J., FE, J., CUETO-FELGUEROSO, L. & JUANES, R. 2012 Scaling of convective mixing in porous media. *Phys. Rev. Lett.* **109** (26), 264503.

HOWARD, L.N. 1966 Convection at high Rayleigh number. In *Proceedings of the 11th International Congress of Applied Mechanics*, pp. 1109–1115. Springer.

HUPPERT, H.E. & NEUFELD, J.A. 2014 The fluid mechanics of carbon dioxide sequestration. *Annu. Rev. Fluid Mech.* **46**, 255–272.

KRAICHNAN, R.H. 1962 Turbulent thermal convection at arbitrary Prandtl number. *Phys. Fluids* **5** (11), 1374–1389.

LETELIER, J.A., MUJICA, N. & ORTEGA, J.H. 2019 Perturbative corrections for the scaling of heat transport in a Hele-Shaw geometry and its application to geological vertical fractures. *J. Fluid Mech.* **864**, 746–767.

LETELIER, J.A., ULLOA, H.N., LEYRER, J. & ORTEGA, J.H. 2023 Scaling CO_2–brine mixing in permeable media via analogue models. *J. Fluid Mech.* **962**, A8.

LIANG, Y., WEN, B., HESSE, M.A. & DICARLO, D. 2018 Effect of dispersion on solutal convection in porous media. *Geophys. Res. Lett.* **45** (18), 9690–9698.

MACMINN, C.W., NEUFELD, J.A., HESSE, M.A. & HUPPERT, H.E. 2012 Spreading and convective dissolution of carbon dioxide in vertically confined, horizontal aquifers. *Water Resour. Res.* **48** (11).

MALKUS, W.V.R. 1954 Discrete transitions in turbulent convection. *Proc. R. Soc. Lond.* A **225** (1161), 185–195.

OTERO, J., DONTCHEVA, L.A., JOHNSTON, H., WORTHING, R.A., KURGANOV, A., PETROVA, G. & DOERING, C.R. 2004 High-Rayleigh number convection in a fluid-saturated porous layer. *J. Fluid Mech.* **500**, 263–281.

PIROZZOLI, S., DE PAOLI, M., ZONTA, F. & SOLDATI, A. 2021 Towards the ultimate regime in Rayleigh–Darcy convection. *J. Fluid Mech.* **911**, R4.

PRIESTLEY, C.H.B. 1954 Convection from a large horizontal surface. *Austral. J. Phys.* **7** (1), 176–201.

SCHRAG, D.P. 2007 Preparing to capture carbon. *Science* **315** (5813), 812–813.

SIMMONS, C.T., FENSTEMAKER, T.R. & SHARP, J.M. JR. 2001 Variable-density groundwater flow and solute transport in heterogeneous porous media: approaches, resolutions and future challenges. *J. Contam. Hydrol.* **52** (1–4), 245–275.

SLIM, A.C. 2014 Solutal-convection regimes in a two-dimensional porous medium. *J. Fluid Mech.* **741**, 461–491.

SONG, J., SHISHKINA, O. & ZHU, X. 2024 Scaling regimes in rapidly rotating thermal convection at extreme Rayleigh numbers. *J. Fluid Mech.* **984**, A45.

SPIEGEL, E.A. 1963 A generalization of the mixing-length theory of turbulent convection. *Astrophys. J.* **138**, 216.

TSINOBER, A., ROSENZWEIG, R., CLASS, H., HELMIG, R. & SHAVIT, U. 2022 The role of mixed convection and hydrodynamic dispersion during CO_2 dissolution in saline aquifers: a numerical study. *Water Resour. Res.* **58** (3), e2021WR030494.

TSINOBER, A., SHAVIT, U. & ROSENZWEIG, R. 2023 Numerical investigation of the influence of hydrodynamic dispersion on solutal natural convection. *Water Resour. Res.* **59**, e2023WR034475.

ULLOA, H.N. & LETELIER, J.A. 2022 Energetics and mixing of thermally driven flows in Hele-Shaw cells. *J. Fluid Mech.* **930**, A16.

VAN DER POEL, E.P., STEVENS, R.J.A.M. & LOHSE, D. 2013 Comparison between two-and three-dimensional Rayleigh–Bénard convection. *J. Fluid mech.* **736**, 177–194.

WEN, B., CHANG, K.W. & HESSE, M.A. 2018 Rayleigh–Darcy convection with hydrodynamic dispersion. *Phys. Rev. Fluids* **3** (12), 123801.

WEN, B., CORSON, L.T. & CHINI, G.P. 2015 Structure and stability of steady porous medium convection at large Rayleigh number. *J. Fluid Mech.* **772**, 197–224.

WEN, B., DIANATI, N., LUNASIN, E., CHINI, G.P. & DOERING, C.R. 2012 New upper bounds and reduced dynamical modeling for Rayleigh–Bénard convection in a fluid saturated porous layer. *Commun. Nonlinear Sci. Numer. Simul.* **17** (5), 2191–2199.

XIA, K.-Q., HUANG, S.-D., XIE, Y.-C. & ZHANG, L. 2023 Tuning heat transport via coherent structure manipulation: recent advances in thermal turbulence. *Natl Sci. Rev.* **10** (6), nwad012.